



# Metastable Helium Absorptions with 3D Hydrodynamics and Self-consistent Photochemistry. I. WASP-69b, Dimensionality, X-Ray and UV Flux Level, Spectral Types, and Flares

Lile Wang<sup>1</sup>  and Fei Dai<sup>2</sup> <sup>1</sup>Center for Computational Astrophysics, Flatiron Institute, New York, NY 10010, USA; [lwang@flatironinstitute.org](mailto:lwang@flatironinstitute.org)<sup>2</sup>Division of Geological and Planetary Sciences, California Institute of Technology, Pasadena, CA 91125, USA

Received 2020 December 18; revised 2021 March 2; accepted 2021 March 23; published 2021 June 21

## Abstract

The metastable helium ( $\text{He}^*$ ) lines near 10830 Å are ideal probes of atmospheric erosion—a common phenomenon of close-in exoplanet evolution. A handful of exoplanet observations yielded well-resolved  $\text{He}^*$  absorption features in transits, yet they were mostly analyzed with 1D isothermal models prescribing mass-loss rates. This work devises 3D hydrodynamics coevolved with ray-tracing radiative transfer and nonequilibrium thermochemistry. Starting from the observed stellar/planetary properties with reasonable assumptions about the host’s high-energy irradiation, we predict from first principles the mass-loss rate, the temperature and ionization profiles, and 3D outflow kinematics. Our simulations well reproduce the observed  $\text{He}^*$  line profiles and light curves of WASP-69b. We further investigate the dependence of  $\text{He}^*$  observables on simulation conditions and host radiation. The key findings are as follows: (1) Simulations reveal a photoevaporative outflow ( $\sim 0.55 M_{\oplus} \text{Gyr}^{-1} \simeq 10^{11} \text{g s}^{-1}$ ) for WASP-69b without a prominent comet-like tail, consistent with the symmetric transit shape. (2) 3D simulations are mandatory for hydrodynamic features, including Coriolis force, advection, and kinematic line broadening. (3) EUV ( $>13.6 \text{eV}$ ) photons dominate photoevaporative outflows and populate  $\text{He}^*$  via recombination; FUV is also detrimental by destroying  $\text{He}^*$ ; X-ray plays a secondary role. (4) K stars hit the sweet spot of EUV/far-UV balance for  $\text{He}^*$  line observation, while G and M stars are also worthy targets. (5) Stellar flares create characteristic responses in the  $\text{He}^*$  line profiles.

*Unified Astronomy Thesaurus concepts:* [Exoplanet atmospheres \(487\)](#); [Exoplanet evolution \(491\)](#); [Exoplanet astronomy \(486\)](#); [Hydrodynamical simulations \(767\)](#); [Astronomical simulations \(1857\)](#); [Hydrodynamics \(1963\)](#); [Astrochemistry \(75\)](#)

## 1. Introduction

One of the most exciting discoveries in exoplanetary sciences in recent years is that the radii of sub-Neptune planets have a bimodal distribution (Fulton et al. 2017). The prevailing explanation is the atmospheric erosion by either photoevaporation (e.g., Owen & Wu 2017) or core-powered mass loss (Ginzburg et al. 2018; Gupta & Schlichting 2019, 2020). In any case, the prominence of the radius gap implies that atmospheric erosion is probably a stage of evolution that close-in exoplanets very commonly go through. Since the discovery of the  $\text{Ly}\alpha$  transit of the hot Jupiter HD 209458b (Vidal-Madjar et al. 2003),  $\text{Ly}\alpha$  has been a workhorse for studying atmospheric erosion (e.g., Lecavelier Des Etangs et al. 2010; Kulow et al. 2014). However,  $\text{Ly}\alpha$  has some unavoidable limitations: it is heavily contaminated by the geocoronal emission and by the interstellar absorption saturating the very center of the line (e.g., Ehrenreich et al. 2015). Moreover, one has to go to the space to observe this UV transition. These effects significantly limit the number of systems for which we can study  $\text{Ly}\alpha$  transits.

Besides  $\text{Ly}\alpha$ , helium lines are emerging as promising outflow indicators. The  $2^3S$  state of helium is often called the “metastable state” ( $\text{He}^*$  hereafter), because the  $2^3S \rightarrow 1^1S$  transition is a magnetic dipole process with a slow spontaneous decay rate of  $A \simeq 1.3 \times 10^{-3} \text{s}^{-1}$  (Drake 1971, 2006). Meanwhile, the transition between the lower  $2^3S$  and the upper  $2^3P_J$  states of helium consists of three lines with  $A > 10^7 \text{s}^{-1}$ , whose wavelengths in vacuum are 10832.08 Å (for the  $J=0$  upper state), 10833.24 Å ( $J=1$ ), and 10833.33 Å ( $J=2$ ) respectively. These lines are often referred to as “He I  $\lambda 10830$  lines” or the “metastable helium

lines,” as they are radiatively decoupled from the ground state. The abundance of helium, the absence of geocoronal or interstellar contamination, the longevity of metastable state, and the observability from the ground together made the  $\text{He}^*$  lines an excellent probe of ionized flows in various scenarios of astrophysics, including quasars (e.g., Leighly et al. 2011), stellar atmospheres and outflows (see Edwards et al. 2003, and references to the article), and T Tauri stars (Kwan et al. 2007).

Over the years, researchers have proposed the  $\text{He}^*$  lines as a tracer of mass loss of close-in exoplanets (Seager & Sasselov 2000; Turner et al. 2016; Oklopčić & Hirata 2018). It was the secured detection of Spake et al. (2018) that revitalized the interest in this unique transition. By the time of the writing this paper, several close-in exoplanets have transmission  $\text{He}^*$  line profiles resolved by ground-based spectrographs (e.g., Allart et al. 2018; Nortmann et al. 2018; Salz et al. 2018; Kirk et al. 2020; Ninan et al. 2020). More recently, Vissapragada et al. (2020) made a narrowband filter specifically for the  $\text{He}^*$  transitions on the diffuser-based photometric system on Palomar/WIRC. The resultant precise light curves of  $\text{He}^*$  are complementary to the line profiles from the near-infrared spectrographs. A lot of information about atmospheric outflow is hiding in these line profiles and light curves are waiting to be interpreted. The models that are commonly used in the literature to interpret these  $\text{He}^*$  observations are 1D spherical symmetric models that are isothermal (Oklopčić & Hirata 2018; Oklopčić 2019; Palle et al. 2020), or have prescribed heating efficiency (Lampón et al. 2020). In comparable works using the EVaporating Exoplanets code (EVE; see also Bourrier et al. 2015; Allart et al. 2018) for the

modeling, an inner isothermal Parker wind is matched to an outer particle-based Monte Carlo model for a complete model of atmospheric outflows. These models are widely recognized for their simplicity and effectiveness. However, they have to prescribe, rather than predict, the mass-loss rates or temperature profiles for the underlying internal atmospheres.

In this work, we build on our previous model that conducts hydrodynamics, self-consistent thermochemistry, and ray-tracing radiative transfer to study the photoevaporation of sub-Neptune planets (Wang & Dai 2018, hereafter **WD18**). We have streamlined the code so that it is sufficiently fast to run in 3D to fully capture the outflow dynamics, and we added various processes that are relevant to the (de)population of  $\text{He}^*$ . We will show in this paper that, using the observed stellar/planetary properties and making reasonable estimates of the high-energy spectral energy distribution (SED) of the host star, our model can predict the mass-loss rate, the temperature profile, and the ionization states and synthesize the observed  $\text{He}^*$  line observables from first principles.

In this first work of a series, we focus on WASP-69b, which is one of the first detections of  $\text{He}^*$  line absorption with a well-resolved line profile (Nortmann et al. 2018). Acknowledging the many limitations of a 1D isothermal model, Nortmann et al. (2018) did not tie their  $\text{He}^*$  line observation to a theoretical model. Instead, they only reported what the data showed directly. Notably, Nortmann et al. (2018) reported an asymmetric transit profile characterized by a longer-than-expected egress that could be caused by a comet-like tail associated with the mass loss. However, Vissapragada et al. (2020) suggest a symmetric shape of transit using better-sampled light curves with higher precision and signal-to-noise ratio. Another interesting point about WASP-69b is the apparent temporal variability of the  $\text{He}^*$  transit depth seen in Nortmann et al. (2018). We will try to understand these observations of WASP-69b in the framework of our 3D hydrodynamic simulations. Afterward, we will use WASP-69b as a fiducial case to investigate the impact of dimensionality, X-ray and ultraviolet (XUV) flux level, and host spectral types on the observables of the  $\text{He}^*$  lines.

This paper is structured as follows. Section 2 describes our methods of numerical simulations and synthetic observations. In Section 3, we present a fiducial model of WASP-69b that well reproduces all current observations. Based on this model, Section 4 studies how various system parameters impact the rate of photoevaporation and  $\text{He}^*$  observables. Section 5 discusses the interpretations of the simulation results and observables. Section 6 summarizes the findings of this paper.

## 2. Methods

### 2.1. Basic Setup

We conceptually divided a planet into four regions: (1) a dense core, (2) a convective inner atmosphere, (3) a quasi-isothermal outer atmosphere with equilibrium temperature  $T_{\text{eq}}$ , and (4) an outflowing region irradiated by high-energy photons (e.g., Rafikov 2006; Ginzburg et al. 2016; Owen & Wu 2016). The equilibrium temperature  $T_{\text{eq}}$  satisfies

$$T_{\text{eq}} \simeq 886 \text{ K} \left( \frac{L_*}{L_{\odot}} \right)^{1/4} \left( \frac{a}{0.1 \text{ au}} \right)^{-1/2}, \quad (1)$$

where  $L_*$  is the bolometric luminosity of the star and  $a$  is the semimajor axis of the planetary orbit. Our simulations will

focus on regions 3 and 4, whereas the structure of regions 1 and 2 provides the correct boundary conditions crucial for correctly reproducing the measured mass and radius of the planet. We refer the reader to the **Appendix** for the details of how we set up the internal structures of our planet and resultant boundary conditions for our simulations.

We characterize the high-energy radiation SED of the host star with five different characteristic energy bins: (1)  $h\nu = 2 \text{ eV}$  for infrared, optical, and near-ultraviolet (NUV) photons; (2)  $h\nu = 7 \text{ eV}$  for “soft” far-ultraviolet (FUV) photons that can photoionize  $\text{He}^*$ ; (3)  $h\nu = 12 \text{ eV}$  for the Lyman–Werner band FUV photons that can photodissociate molecular hydrogen; (4)  $h\nu = 20 \text{ eV}$  for “soft” extreme-ultraviolet (soft EUV) photons that can ionize hydrogen but *not* helium; (5)  $h\nu = 40 \text{ eV}$  for hard EUV photons that ionize hydrogen *and* helium; and (6)  $h\nu = 3 \text{ keV}$  for the X-ray.

Our simulation combines ray-tracing radiative transfer, real-time nonequilibrium thermochemistry, and full hydrodynamics calculations (based on a higher-order Godunov hydrodynamic solver `Athena++`; Stone et al. 2020). The simulation is mostly based on our **WD18** work, with a few modifications and improvements added for the higher dimensionality and the inclusion of  $\text{He}^*$ .

### 2.2. Geometry and Boundary Conditions

The density distribution, temperature profile, and dynamics of the outflowing atmosphere all play a part in the  $\text{He}^*$  observables. To capture the outflow dynamics accurately, simulations should include the gravity of the star and the planet and the effects of orbital motion: the centrifugal and Coriolis forces. Therefore, 3D simulations are required. Given its short orbital period and observed radial velocities (Anderson et al. 2014), we assume that WASP-69b is tidally locked and circularized. Our simulation is run in a corotating frame centered on the planet. We adopt a spherical polar coordinate  $(r, \theta, \phi)$  with  $\theta = 0$  pointing toward the host star and  $\phi = 0$  pointing in the direction of orbital motion.

The mesh covers the domain  $(r, \theta, \phi) \in [r_{\text{in}}, r_{\text{out}}] \otimes [0, \pi] \otimes [0, \pi]$ . Planet-specific radial boundaries  $r_{\text{in}}$  and  $r_{\text{out}}$  usually extend from the base of the quasi-isothermal layer to a relatively large radius ( $150 R_{\oplus}$  in this case) such that the density/opacity drops low enough. The radial grids are placed logarithmically to strategically capture the steep change of density, while latitudinal and azimuthal grids are spaced evenly. Reflecting boundary conditions are enforced at the  $r = r_{\text{in}}$ ,  $\phi = 0$ , and  $\phi = \pi$  boundaries, while the  $r = r_{\text{out}}$  boundary is an outflowing boundary. The  $\theta = 0$ ,  $\theta = \pi$  boundaries are polar wedges to avoid coordinate singularity. The whole mesh, with its polar axis always pointing toward the host star, corotates with the orbital motion and the rotation of the tidally locked planet.

In a 3D spherical polar mesh, the grids near the polar axis are narrow in the azimuthal direction ( $\delta x_{\phi} \simeq r_{\text{cc}} \sin \theta_{\text{cc}} \delta \phi$ ; subscripts “cc” stand for “cell center”). This can result in highly nonunitary aspect ratios ( $\delta x_{\theta} \simeq r_{\text{cc}} \delta \theta$ ) and a stringent Courant–Friedrichs–Lewy (CFL) condition. We thus introduce an adaptive “mesh coarsening” technique for the azimuthal grids near the poles. Without any violations of conservation laws, the effective aspect ratio of the high-latitude zones becomes close to 1 and the time-step constraints imposed by the CFL condition are not as severe (see also Nakamura et al. 2019; Müller et al. 2019). This helps to greatly speed up our model.

### 2.3. $\text{He}^*$ in Non-LTE Thermochemistry

Our simulation includes a non-LTE reaction network that coevolves with the hydrodynamics (see [WD18](#) for details), with the addition of the metastable state of neutral helium and all relevant reactions that populate and depopulate this state (see [Oklopčić & Hirata 2018](#) and references therein). Our reaction network now has 26 thermochemical “species” that are considered important to the thermochemistry of photoevaporation, including  $\text{He}^*$  and internal energy density,<sup>3</sup> and 135 reactions such as ionization, recombination, collisional (de-) excitation, photodissociation, and cooling and heating processes. The reaction network includes processes that are directly relevant to photoevaporation, including photoionization and photodissociation heating, the dust–gas thermal accommodation, recombination cooling, and collision–radiation cooling especially by the species containing carbon, oxygen, silicon, and sulfur (see, e.g., [Tielens & Hollenbach 1985](#); [Gorti & Hollenbach 2008](#); [Gong et al. 2017](#); [Wang & Goodman 2017](#); [WD18](#)). The ordinary differential equations (ODEs) of the thermochemical network were solved efficiently using the semi-implicit method specially optimized for the graphics processing units (GPUs). The resultant efficiency allows us to coevolve the hydrodynamics with the thermodynamics, rather than including thermodynamics as a post-processing step that is often done in the literature. Again, we refer interested readers to [WD18](#) for more details.

### 2.4. Synthetic Observations

We synthesize both the transmission line profiles ([Nortmann et al. 2018](#)) and the narrowband light curves ([Vissapragada et al. 2020](#)) of  $\text{He}^*$  transitions using our simulations. At each wavelength  $\lambda$  and a particular orbital phase, the optical depth along a line of sight (LOS) is given by

$$\tau(\lambda; \Phi) = \int |d\mathbf{x}| n(\text{He}^*; \mathbf{x}; \Phi) \times \sigma_i[\lambda; \hat{n}_{\text{LoS}} \cdot \mathbf{v}(\mathbf{x}; \Phi), T(\mathbf{x}; \Phi)], \quad (2)$$

where we have transformed from our planet-centered coordinate systems in the simulations to a star-centered coordinate system for the synthetic observations. Thus,  $\mathbf{x}$  and  $\mathbf{v}$  are the position and velocity vector measured from the host star. The integration goes along the designated LOS, and the summation index  $i$  runs over the three  $\text{He}^*$  lines with different upper-state quantum number  $J$ . The cross section  $\sigma_i$  is assumed to be a Voigt profile that convolves the intrinsic Lorentzian profile ( $\gamma = A/4\pi$ ,  $A = 1.0216 \times 10^7 \text{ s}^{-1}$ ; see [Drake 2006](#)) with a Gaussian profile from thermal broadening at temperature  $T(\mathbf{x})$ . This Voigt profile is shifted by the local bulk velocity including orbital motion and outflow kinematics and the projection onto the LOS  $\hat{n}_{\text{LoS}} \cdot \mathbf{v}(\mathbf{x})$ .

This integration is performed for all relevant LOSs that originate from the surface of the host star:

$$\epsilon(\lambda; \Phi) = 1 - \int d\Sigma S e^{-\tau(\lambda; \Phi)}, \quad (3)$$

<sup>3</sup> The thermochemical “species” are  $e^-$  (free electrons),  $\text{H}^+$ ,  $\text{H}$ ,  $\text{H}_2$ ,  $\text{H}_2^*$  (proxy for molecular hydrogen in vibrational excited state; see also [Tielens & Hollenbach 1985](#)),  $\text{He}$ ,  $\text{He}^+$ ,  $\text{He}^*$ ,  $\text{O}$ ,  $\text{O}^+$ ,  $\text{O}^*$  (proxy for all neutral excited oxygen),  $\text{OH}$ ,  $\text{H}_2\text{O}$ ,  $\text{C}$ ,  $\text{C}^+$ ,  $\text{CO}$ ,  $\text{CH}$ ,  $\text{CH}^+$ ,  $\text{S}$ ,  $\text{S}^+$ ,  $\text{Si}$ ,  $\text{Si}^+$ ,  $\text{Gr}$ ,  $\text{Gr}^+$ ,  $\text{Gr}^-$ , and internal energy density. Here  $\text{Gr}$  and  $\text{Gr}^\pm$  denote neutral and singly charged dust grains, respectively.

where  $\epsilon(\lambda)$  is the relative extinction at wavelength  $\lambda$ , and  $S(\lambda)$  is the normalized surface brightness ( $\int d\Sigma S(\lambda) = 1$ ) of the star after accounting for limb darkening and stellar rotation. The integral runs through the entire projected stellar surface.

$\epsilon(\lambda; \Phi)$  is the absorption-line profile as a function of wavelength and orbital phase (time). We mimic what observers often do in  $\text{He}^*$  observations, i.e., time averaging  $\epsilon(\lambda; \Phi)$  over the entire transit event from nominal ingress to egress ( $t_{\text{in}}$  through  $t_{\text{out}}$ ).<sup>4</sup> The outcome  $\Delta\epsilon(\lambda)$  is a line profile of excess absorption to be compared with observations directly.

We report a number of summary statistics, including the equivalent widths (EWs)  $\langle W_\lambda \rangle \equiv \int \Delta\epsilon(\lambda) d\lambda$ , the radial velocity shift of the absorption peak  $\Delta v_{\text{peak}}$ , and the FWHM of the absorption-line profile. These summary statistics help us to compare between models and observations efficiently and are less prone to measurement uncertainty, bad pixels, and other instrumental effects.

Finally, we integrated  $\epsilon(\lambda; \Phi)$  multiplied by a filter bandpass function over  $\lambda$ . The result is a transit light curve near the  $\text{He}^*$  transitions. In this work, we use the bandpass function provided by [Vissapragada et al. \(2020\)](#) for a direct comparison with their results.

## 3. Fiducial Model of WASP-69b

In this section, we will show how we arrived at a fiducial model that gives rather remarkable agreement with the observed  $\text{He}^*$  line profiles ([Nortmann et al. 2018](#)) and light curves ([Vissapragada et al. 2020](#)). We note that our 3D hydrodynamic model is not fast enough<sup>5</sup> for a full exploration of the parameter space with techniques such as Markov Chain Monte Carlo or even simple gradient descent. Instead, we had to rely on the reported system parameters and making reasonable assumptions, as well as hand-tuning the high-energy SED of the host star. We will see shortly, without much tuning, that we can arrive at a fiducial model that fits various observations of WASP-69b very well.

We set up our simulations to match the reported system properties of WASP-69b ([Anderson et al. 2014](#)). The host star is a K star with  $M_* = 0.826 M_\odot$ ,  $R_* = 0.813 R_\odot$ , and  $T_{\text{eff}} = 4715 \text{ K}$ . WASP-69b has a circular orbit with semimajor axis  $a = 0.04525 \text{ au}$ . The equilibrium temperature is estimated using Equation (1),  $T_{\text{eq}} = 965 \text{ K}$ . The planet has an optical transit radius of  $R_p \simeq 1.057 R_{\text{Jup}}$  and a mass of  $M_p \simeq 0.26 M_{\text{Jup}}$  from radial velocity follow-ups. Details of the fiducial model are presented in Table 1.

The interior of our WASP-69b model is set up as described in the [Appendix](#). The core size, the equation of state (EOS), and other details of the interior of a giant planet are still subject to a lot of uncertainties even in the case of Jupiter (see, e.g., [Wahl et al. 2017](#)). However, the details of the interior should not affect the outflowing region of the envelope, which is what we are interested in in this work. We set the inner boundary of our simulation at  $11.37 R_\oplus$  so that we capture several scale heights below the optical transit radius ( $r_{\text{eff}} \simeq R_p$  at  $1.057 R_{\text{Jup}}$ ). The outer boundary is located at  $150 R_\oplus$ . For simplicity, we assumed an atmospheric metallicity often seen in

<sup>4</sup> Following the conventions, in this paper we use  $t_1$  and  $t_{\text{in}}$  for the start/end of the ingress and  $t_{\text{out}}$  and  $t_{\text{iv}}$  for those of the egress.

<sup>5</sup> Even with a GPU-accelerated infrastructure, each simulation takes about 5 hr on one computation node with 40 CPU cores (Intel Skylake) and four GPUs (Nvidia Tesla V100) on the Popeye-Simons Computing Cluster.

**Table 1**  
Properties of the Fiducial Model for WASP-69b

Item	Value
Planet interior <sup>a</sup>	
$M_{\text{rcb}}$	$82.6 M_{\oplus} (\simeq 0.26 M_J)^b$
$\langle r_{\text{eff}} \rangle$	$11.8 R_{\oplus} (\simeq 1.05 R_J)^b$
Simulation domain	
Radial range	$11.37 \leq (r/R_{\oplus}) \leq 150$ $[0.96 \leq (r/\langle r_{\text{eff}} \rangle) < 12.7]$
Latitudinal range	$0 \leq \theta \leq \pi$
Azimuthal range	$0 \leq \phi \leq \pi$
Resolution ( $N_{\log r} \times N_{\theta} \times N_{\phi}$ )	$144 \times 128 \times 64$
Radiation flux (photons $\text{cm}^{-2} \text{s}^{-1}$ )	
2 eV (IR/optical)	$6.4 \times 10^{19}$
7 eV (soft FUV)	$6 \times 10^{15}$
12 eV (LW)	$1 \times 10^{12}$
20 eV (soft EUV) <sup>c</sup>	$5 \times 10^{12}$
40 eV (hard EUV) <sup>c</sup>	$3 \times 10^{13}$
3 keV (X-ray) <sup>c</sup>	$1.2 \times 10^{12}$
Initial abundances [ $n_X/n_H$ ]	
H <sub>2</sub>	0.5
He	0.1
H <sub>2</sub> O	$1.8 \times 10^{-4}$
CO	$1.4 \times 10^{-4}$
S	$2.8 \times 10^{-5}$
Si	$1.7 \times 10^{-6}$
Gr	$1.0 \times 10^{-7}$
Dust/PAH properties	
$\sigma_{\text{dust}}/H$ (effective specific cross section)	$8 \times 10^{-22} \text{ cm}^2$

#### Notes.

<sup>a</sup> See the [Appendix](#); Thomson opacity is used for  $\langle r_{\text{eff}} \rangle$ .

<sup>b</sup> Mass and radius of Jupiter.

<sup>c</sup> The inferred values of fluxes in Nortmann et al. (2018) for WASP-69b are  $2.6 \times 10^{13} \text{ photons cm}^{-2} \text{ s}^{-1}$  for EUV (represented by  $h\nu = 40 \text{ eV}$  photons) and  $0.5 \times 10^{12} \text{ photons cm}^{-2} \text{ s}^{-1}$  for X-ray (represented by  $h\nu = 3 \text{ keV}$  photons).

protoplanetary disks (WD18) that is slightly below the solar value (Table 1). It is noteworthy that Tsiaras et al. (2018) reported an abundance of water in the atmosphere of WASP-69b close to the value we adopt in the table ( $10^{-3.94 \pm 1.25}$  volume mixing ratio). This value, nonetheless, does not necessarily represent the metal abundance, since the water molecules can be dissociated by the stellar irradiation. We will explore any metallicity dependence in a future work when more dedicated observation data are available.

Optical and infrared fluxes, represented by the  $h\nu = 2 \text{ eV}$  photon energy bin, are calculated using the host star radius and effective temperature. For the high-energy photons, more uncertainties are involved depending on the age/activity of the host star, while direct measurements are also lacking. We note that WASP-69 is moderately active as indicated by the Ca II H and K lines  $\log R'_{\text{H,K}} = -4.54$  (Anderson et al. 2014). As we will see later in Section 4.2, the He\* absorption-line profile depends critically on the shares taken by various high-energy radiation bins. After gaining intuition on how each energy bin affects the He\* line profiles (again Section 4.2), we varied the high-energy SED of WASP-69 until we achieved a reasonable agreement with both the line profile and light-curve measurements. The resultant high-energy SED is quite typical of a K5 star when compared to the observational constraint of FUV and EUV flux of the MUSCLES survey (France et al. 2016; Youngblood et al. 2016; Loyd et al. 2016; Youngblood et al. 2017), the X-ray

flux according to Gudel (1992), and the more comprehensive compilation of Oklopčić (2019).

### 3.1. A Photoevaporative Outflow on WASP-69b

Before analyzing our simulations, we ensured that quasi-steady states have been achieved. This usually involved running the simulations for many dynamical timescales; specifically, we set  $t_{\text{sim}} \gtrsim 30 \tau_{\text{dyn}}$ . The dynamical timescale  $\tau_{\text{dyn}}$  is estimated by the sound-crossing time of the Bondi radius:

$$\tau_{\text{dyn}} \sim \frac{GM_p}{c_s^3} \sim 1.2 \times 10^3 \text{ s} \times \left( \frac{M_p}{10 M_{\oplus}} \right) \left( \frac{T}{10^4 \text{ K}} \right)^{-3/2}. \quad (4)$$

Here  $c_s$  is the sound speed. For a typical  $T = 10^4 \text{ K}$  outflow we see for WASP-69b  $\tau_{\text{dyn}} \sim 10^4 \text{ s}$ . Moreover, we also check explicitly whether the simulation has settled down to a quasi-steady state by comparing key hydrodynamic/thermodynamic properties in neighboring dump files.

Our fiducial model for WASP-69b shows clear signs of a photoevaporative outflow. In Figure 1, we show 2D slices of the density, temperature, and LOS velocity distributions of our 3D simulations looking down the north pole of the planet. We see a  $T \gtrsim 10^4 \text{ K}$  hot ionized supersonic outflow originating at a wind base of  $r \simeq 13 R_{\oplus}$ , which eventually accelerates to  $\sim 23 \text{ km s}^{-1}$  when leaving the domain of our simulation. This outflow disperses the planet atmosphere at a mass-loss rate of  $\dot{M} \simeq 5.5 \times 10^{-10} M_{\oplus} \text{ yr}^{-1}$ . Since we assumed a constant high-energy radiation output from the host star, the mass-loss rates and the hydrodynamic/thermodynamic profiles remain nearly constant after reaching the quasi-steady state. We also note that we did not put in any stellar wind from the host star, as the current windless model fits the data reasonably well and is preferred by Occam's razor. However, in a companion paper on WASP-107 we will show that stellar winds may generate Kelvin–Helmholtz instability that leads to fluctuations of a photoevaporative outflow.

Which mechanisms control the population of the He\* state? The bottom row in Figure 2 compares the rates of different (de)population processes along the two particular streamlines (thickened curves in Figure 1). We compute the rate of ionization, recombination, spontaneous decay, collisional excitation, and de-excitation, as well as an advection attenuation term  $|\mathbf{v} \cdot \nabla n(\text{He}^*)|$ . Along the representative streamline presented by the left column, the abundance of He\* is determined by the relatively stiff balance between the recombination ( $\text{He}^+ + \text{e}^- \rightarrow \text{He}^*$ ) and the collisional de-excitation at small radii  $\lesssim 30 R_{\oplus}$ . As expected, these two processes are efficient at higher densities, consistent with the law of mass action. Photoionization of He\* by soft FUV starts to take over the destruction channel of He\*, where the density of free electrons declines at higher altitudes. The other channels have negligible importance, e.g., collisional excitation from  $1^1S$  to the metastable state is more than five orders of magnitude slower than recombination. In the right column of Figure 2, we show an interesting streamline that crosses in the shadow of the planet. The number density of He\* soars in the shadow because the photoionization of He\* by soft FUV vanishes here.

Beneath the base of the photoevaporative outflow ( $r \lesssim 13 R_{\oplus}$ ), the temperature gradient between the dayside and the nightside generates a slow “zonal” circulation ( $\sim 0.1 \text{ km s}^{-1}$ ). However, this region has little observational effect on the overall He\*\*

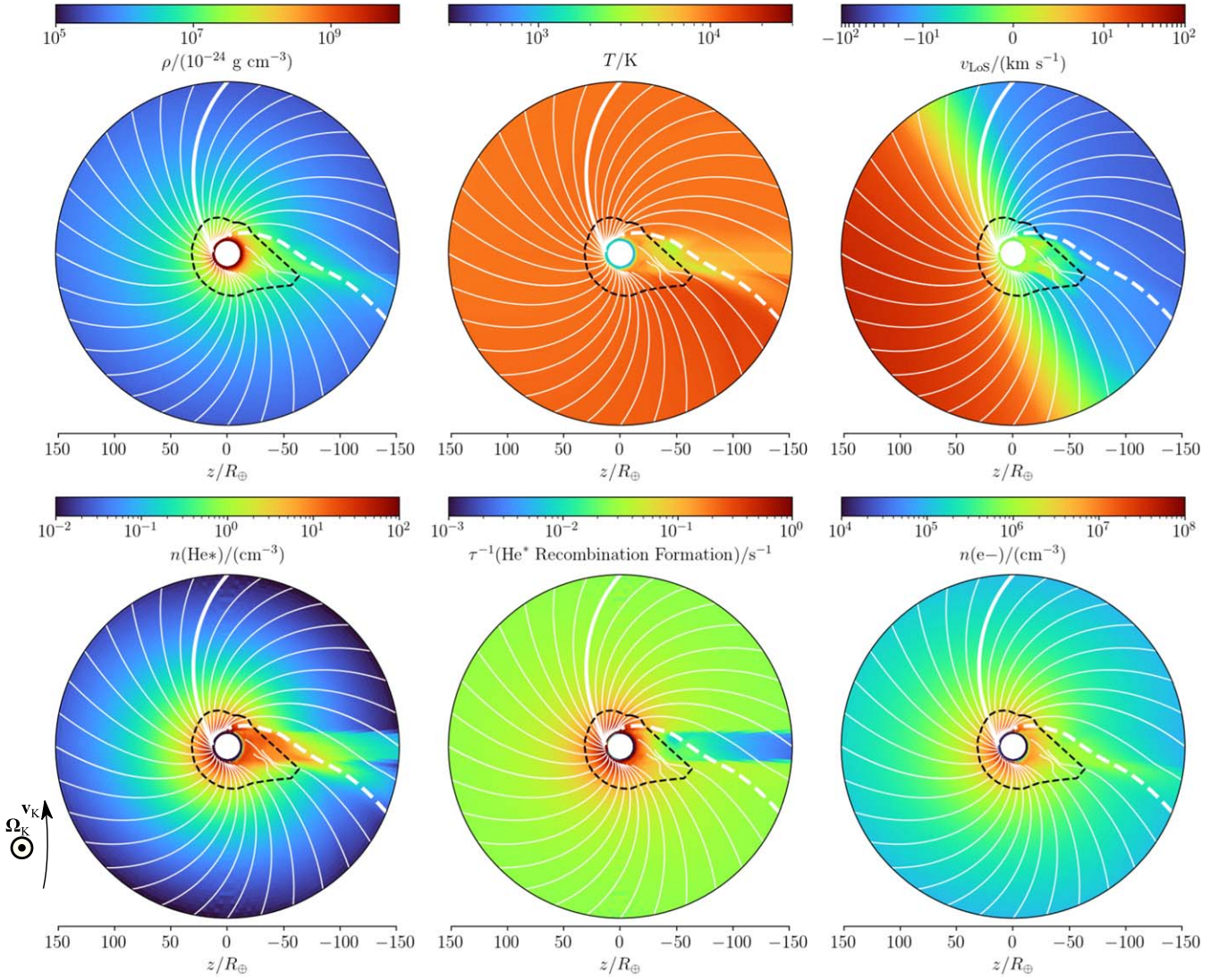


**Figure 1.** Profiles of the simulation for WASP-69b (fiducial model 69-0) in its quasi-steady state. Stellar radiation comes from the left of the plot, and the orbital angular velocity  $\Omega_K$  points out of the paper plane; the Keplerian motion of the planet is upward  $v_K$ . Color maps show the mass density  $\rho$  (top left panel), temperature  $T$  (top middle), LOS velocity  $v_{\text{LOS}}$  (top right; the values are measured at midtransit), He\* number density  $n(\text{He}^*)$  (bottom left), inverse timescale of recombination He\* formation (defined as formation rate normalized by  $n(\text{He}^*)$ ; bottom middle), and free electron number density  $n(e^-)$  (bottom right). White streamlines (projected to the orbital plane) are overlaid on each panel; two neighbor streamlines are separated in such a way that they are  $\Delta\theta = \pi/16$  apart when they reach the outer radial boundary ( $r = 150 R_\oplus$ ). The heavy streamlines are the reference lines on which the profiles are plotted in Figure 2. Black dashed lines indicate the sonic surface.

observables, which are mostly controlled by the much more extended low-density regions of the outflowing atmosphere. We will return to this point shortly. Moving to higher altitude, this day–night advection continues, amounting to a 2–3  $\text{km s}^{-1}$  blueshift at about 20–40  $R_\oplus$ . Going farther away from the planet, the Coriolis effect starts to shape the outflow streamlines into spiral curves, resulting in blueshifts on the leading edge and redshifts on the trailing edge. Considering that the outflow is still primarily radial, increments in the latitudinal velocity  $|\Delta v_\theta|$  after traveling through a radial distance  $\Delta r$  can be estimated by

$$\begin{aligned} \Delta v_\theta &\sim 2 \cos \phi \Omega_K \int dt v_r \simeq 2 \cos \phi \Omega_K \Delta r \\ &\simeq 2.3 \text{ km s}^{-1} \cos \phi \left( \frac{M_*}{M_\odot} \right)^{1/2} \\ &\quad \times \left( \frac{a}{0.05 \text{ au}} \right)^{-3/2} \left( \frac{\Delta r}{10 R_\oplus} \right). \end{aligned} \quad (5)$$

This estimation is confirmed by the velocity profile in the top panels of Figure 2: if we compare the values at  $r \simeq 40 R_\oplus$  and  $r \simeq 100 R_\oplus$ , the difference in  $v_{\text{LOS}}$  (approximately equal to  $v_\theta$  for this streamline) is  $\Delta v_{\text{LOS}} \sim 11 \text{ km s}^{-1}$ , and Equation (5) yields  $\sim 10.8 \text{ km s}^{-1}$ . This effect redistributes He\* atoms in the velocity space and broadens the observed He\* line profiles as we will see shortly.

### 3.2. Comparison with Observations

Figure 3 shows our synthetic observations of both the line profiles and light curves of WASP-69b (Nortmann et al. 2018; Vissapragada et al. 2020). We have binned the light-curve data from Vissapragada et al. (2020) for better clarity, and the uncertainty represents the standard deviation within each phase bin. Our fiducial model of WASP-69 seems to fit both the spectroscopic and photometric observations well simultaneously. In particular, the synthetic line profile reproduced

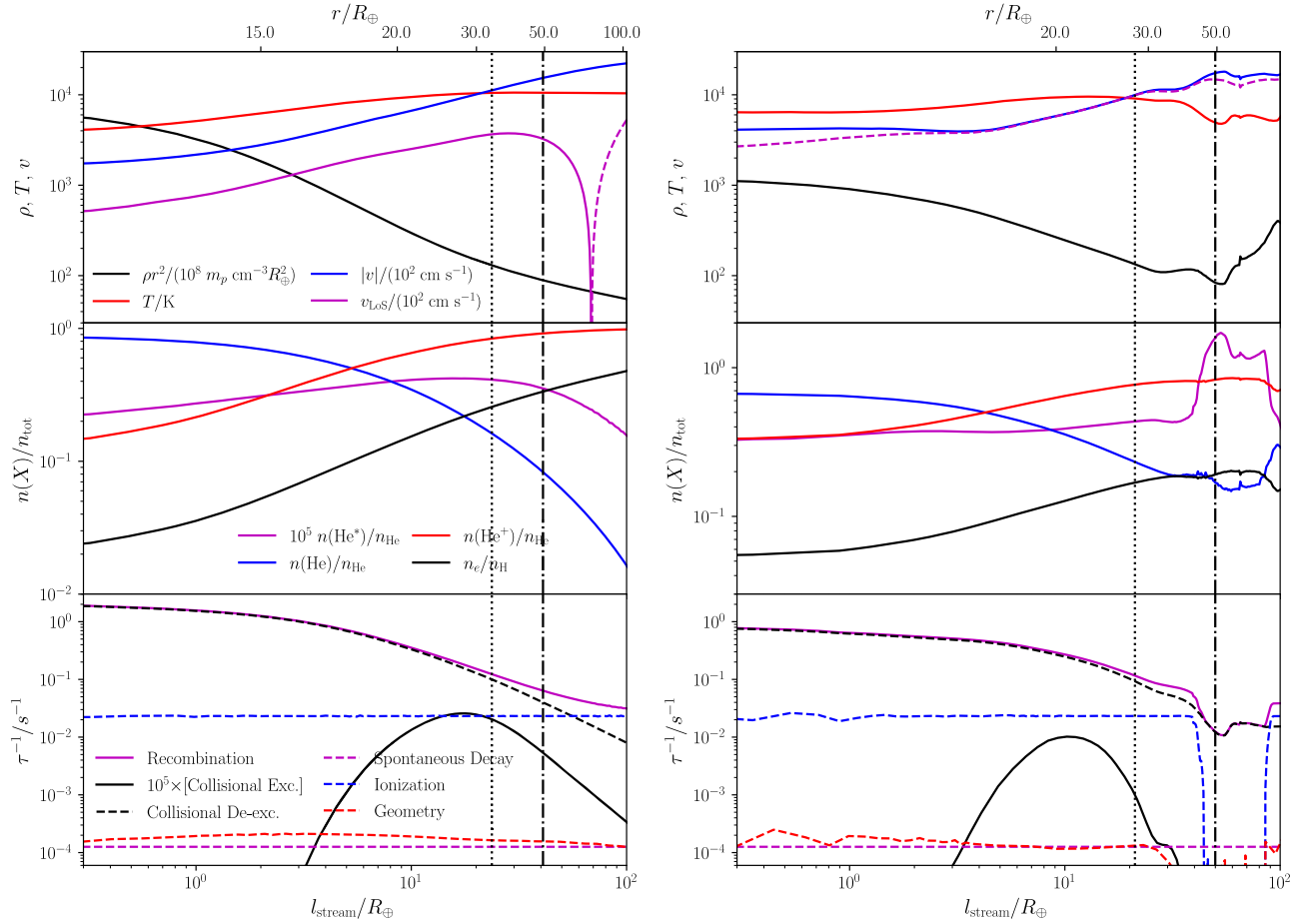


**Figure 2.** Key quantities of our fiducial model for WASP-69b (model 69-0) along the two reference streamlines (plotted as the thick streamlines in Figure 1). The top abscissa is the radial coordinate  $r$  corresponding to the curve length along the streamline on the bottom abscissa. The top panels contain the profiles of scaled mass density  $\rho^2$ , temperature  $T$ , velocity magnitude  $|v|$ , and LOS velocity  $v_{\text{LOS}}$ . The dashed part of the  $v_{\text{LOS}}$  curve indicates negative values. The middle panels present the abundances of free electrons (relative to total hydrogen nucleus density  $n_{\text{H}}$ ) and helium in different forms (relative to the total helium nucleus density  $n_{\text{He}}$ ; note that  $n(\text{He}^*)$  is multiplied by  $10^5$  for clarity). Inverse timescales of  $\text{He}^*$  formation (in solid curves; note that the collisional excitation rate is multiplied by  $10^5$ ) and destruction (in dashed curves) processes are shown in the bottom panels. In all panels, the vertical dotted line indicates the sonic critical point, and the vertical dashed-dotted line shows the location of the Roche radius.

the subtle blueshift of the peak absorption, the overall line depth, and the relative ratio between the lines of this triplet. Numerically, Nortmann et al. (2018) reported a net blueshift of  $-3.58 \pm 0.23 \text{ km s}^{-1}$ . This blueshift was based on fitting Gaussians to the observed line profiles; however, as we argued in the previous section, kinematic shift of the outflow introduces significant distortion of the spectral shape. Instead of fitting a Gaussian to our line profile, we compared our simulations directly to the line profile itself, which shows great agreement. We also use a different way to measure the blueshift: we report the blueshift of the peak absorption relative to a line-ratio-weighted average of the rest-frame line center for the two longer-wavelength transitions that are usually blended together.

Nortmann et al. (2018) hinted at the possibility of a comet-like tail trailing behind WASP-69b. The basis of their suggestion is that additional  $\text{He}^*$  absorption can still be seen  $\sim 20$  minutes after the nominal egress of the planet. The higher-precision, better temporally sampled photometric data from Vissapragada et al. (2020) nonetheless favor a symmetric transit. The symmetric transit shape (bottom panel of Figure 3) does not support an extended comet-like tail. Our simulation seems to be more consistent with Vissapragada et al. (2020); the photoevaporative outflow of WASP-69b in our fiducial

model is largely symmetric between the leading and trailing edge, and hence it produces a more symmetric transit shape. We note that an extended comet-like tail will also introduce significant distortion to the  $\text{He}^*$  line profile (see our companion paper on WASP-107b for the strong comet-like tail generated by strong stellar wind in that system). Here in the case of WASP-69b, our fiducial model produces a good fit to the resolved line profile (Nortmann et al. 2018), while it does not need to invoke a prominent comet-like tail.

Another point we would like to emphasize is that a significant part of the  $\text{He}^*$  absorption for WASP-69 seems to be produced by an extended, optically thin ( $\tau < 1$ ) outer layer of the photoevaporative outflow. In Figure 4, we show the midtransit extinction ( $1 - \exp^{-\tau}$ ) at three different wavelengths near the  $\text{He}^*$  transitions. The outer regions (tens of  $R_{\oplus}$ ) contribute significantly to the overall extinction thanks to their extended area and the slow decrease of  $\text{He}^*$  number density in the outflow. Because of the unsaturated optical depth, the line ratios between the  $\text{He}^*$  triplet are close to 1:3:5, i.e., their quantum degeneracies. More accurately, the line ratios are close to 1:8, as the longer two lines are blended by kinematics and thermal broadening. This suggests that the line ratios between the  $\text{He}^*$  triplet can be a diagnostic of the number density in the outflow. If most of the  $\text{He}^*$  absorption is due to the higher-density region, where one of the

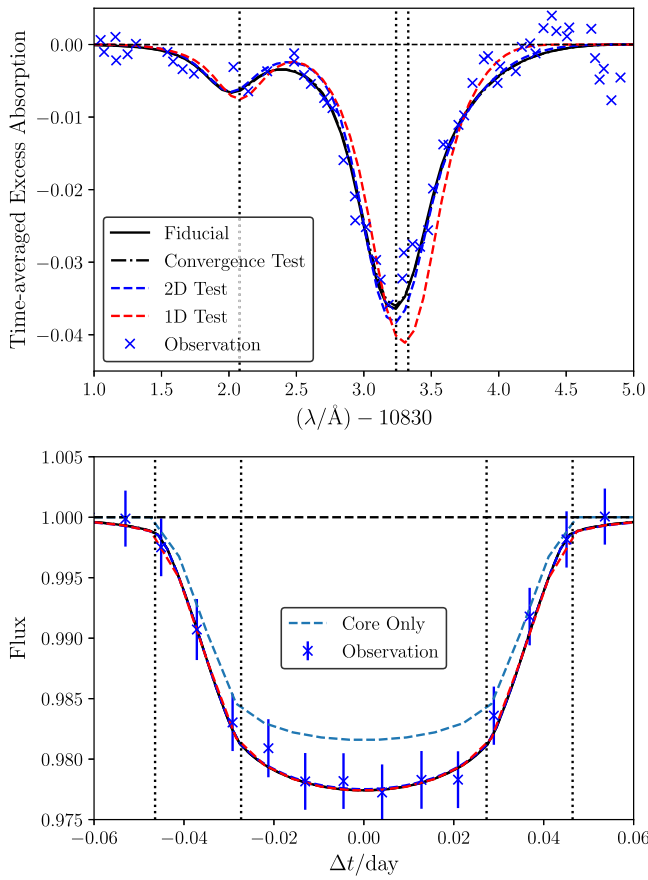


**Figure 3.** Observed and synthesized line profiles and light curves for WASP-69b. We include the results of our fiducial model (3D), 2D test, 1D test, and a convergence test (same as the fiducial but has a higher spatial resolution; Section 2.1), with different line styles. Note that the curves for some test models overlap the fiducial curve and cannot be distinguished. The top panel presents the time-averaged excess absorption transmission spectra or the resolved line profile (Equation (3)); time-averaged from the end of ingress through the beginning of egress). Three vertical dotted lines indicate the three central wavelengths of the He<sup>\*</sup> triplet. The bottom panel compares the synthesized light curve with the observations and a hypothetical planet that *does not* have any atmospheres. We have rebinned the light-curve data in Vissapragada et al. (2020). The four vertical dotted lines indicate the ingress and egress.

lines may saturate first, the line ratio will deviate from the quantum degeneracy ratio; this would tell us about the density of the outflow region in a model-independent way (see also discussions in Salz et al. 2018). This does not seem to be the case for WASP-69b, as most He<sup>\*</sup> absorption happens in lower-density regions. Another feature revealed by Figure 4 is that the leading edge tends to be bluer and the trailing edge redder. This is consistent with the Coriolis effects (Section 3.1) and reiterates the importance of multidimensional studies to consistently understand the spectral profiles.

It is worth noting that, due to the heavy computational cost of our 3D simulations, we could not afford to numerically fit the data with multiple simulation runs. Instead, our fiducial model serves as a validation of our self-consistent 3D hydrodynamic simulations: with reasonable assumptions of the planetary and stellar properties (such as the high-energy SED), we can at least qualitatively reproduce the various He<sup>\*</sup> observables. The degree to which our simulation agrees with observations is quite encouraging if not remarkable. After this validation of the model, we stand at a position to perturb our

fiducial model and investigate how the He<sup>\*</sup> observables are impacted by various factors that control the underlying photoevaporative outflow and He<sup>\*</sup> population in the following section.

## 4. Parametric Study

How do the photoevaporative outflow and the resultant He<sup>\*</sup> observables depend on key parameters in our simulations? In this section, we explore the impact of simulation dimensionality, XUV flux levels, host star spectral type, and planet surface gravity. This is done by perturbing the validated fiducial model in these parameters. Before that, we did a further convergence test. We reran the fiducial model with a much finer simulation grid of  $N_{\log r} \times N_{\theta} \times N_{\phi} = 192 \times 192 \times 128$  (versus the fiducial model,  $N_{\log r} \times N_{\theta} \times N_{\phi} = 144 \times 128 \times 64$ ). The resultant He<sup>\*</sup> observables in the convergence test are almost identical (Figure 3) to the much faster fiducial model. This gives us confidence that the adopted spatial grid is fine enough to resolve the photoevaporative outflow on WASP-69b.

### 4.1. Dimensionality

To test how our model depends on the spatial dimensions of the simulations, we ran a 2D model with axisymmetry (about the  $\phi$ -axis, i.e.,  $N_{\phi} = 1$ ) while keeping all system parameters the same as the fiducial model. The Coriolis force is not captured in this 2D simulation while stellar gravity and orbital centrifugal forces are still involved. A reference 1D spherical symmetric model is also implemented using the  $\theta = \pi/2$ ,  $\phi = \pi/2$  radial line and removing the  $\theta$  and  $\phi$  components of the velocity.

Figure 3 compares the synthesized line profiles and light curves with all three-dimensionality models. The 1D spherically symmetric model suffers from the loss of all nonradial kinematic information. It is clearly inconsistent with the observed line profile with no blueshift and limited kinematic broadening. The 2D axisymmetric test is able to capture the day-night advection. It shows good agreement with the observed line profile. The 3D fiducial model further modifies the line profile by including the Coriolis force. In the case of WASP-69b such a modification is quite subtle, which again testifies that the photoevaporative outflow on WASP-69b is largely symmetric between the leading and trailing edge. Again see our companion paper on WASP-107b for how this symmetry is broken by the inclusion of stellar winds.

The three models from 1D through 3D have almost identical EW ( $\langle W_{\lambda} \rangle \sim 3.1 \text{ \AA}$ ) and light curves. This stresses the importance of spectrally resolving the He<sup>\*</sup> line profiles that are seen to vary the most between dimensions. The mass-loss rates are again quite similar between 3D and 2D models at about  $\dot{M} \simeq 5.5 \times 10^{-10} M_{\oplus} \text{ yr}^{-1}$ . The mass-loss rate in our 1D model is off ( $\dot{M} \simeq 6.9 \times 10^{-10} M_{\oplus} \text{ yr}^{-1}$ ) because it assumes perfect spherical symmetry. However, the streamlines in Figure 1 are clearly nonradial. We also compare our results with those from a 1D isothermal model (Oklopčić & Hirata 2018; Vissapragada et al. 2020) of  $9.5 \times 10^{-10} M_{\oplus} \text{ yr}^{-1}$  ( $\simeq 3 \times 10^{-3} M_{\text{Jup}} \text{ Gyr}^{-1}$ ) at an assumed temperature of 12,000 K. The results are in rough agreement with differences arising from more careful treatment of the hydrodynamics, thermodynamics, and radiative transfer.

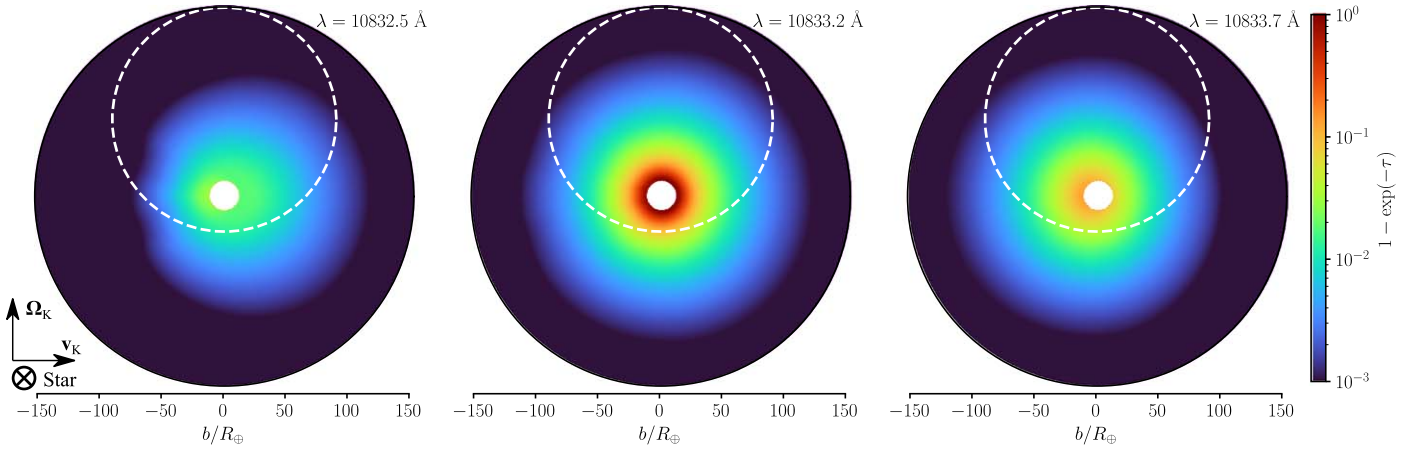


**Figure 4.** Extinction  $[1 - \exp(-\tau)]$  for model 69-0 at three representative wavelengths  $(\lambda/\text{\AA}) \in \{10832.5, 10833.2, 10833.7\}$  near the  $\text{He}^*$  transitions. The profiles are measured at midtransit (viz., all LOSs are parallel to the star–planet line) and in a frame centered at the planet. The white dashed circles indicate the projected host star (with reported stellar radius and orbital inclination). The direction of orbital motion ( $\mathbf{v}_k$ ), direction of the orbital angular momentum vector ( $\mathbf{\Omega}_k$ ), and direction to the host star are indicated in the lower left corner of the whole figure.

#### 4.2. XUV Flux Intensity

Photoevaporative outflows are driven by high-energy radiation from the host star. Moreover, the population of  $\text{He}^*$  states is also controlled by the critical balance high-energy photons of different energy bins. We examine the impact of high-energy radiation in each energy bin by perturbing the fiducial model. The amount of high-energy radiation a star outputs is variable depending on the evolution stage, activity, and spectral types of the host star. Direct measurements are also lacking, as the XUV measurements have to be performed in space. Therefore, in our models 69-1 to 69-5 (soft FUV for 69-1, LW for 69-2, soft EUV for 69-3, hard EUV for 69-4, X-ray for 69-5), we bump up the flux level in each high-energy bin by a whole order of magnitude to reflect the intrinsic variation in high-energy flux level. We summarize key  $\text{He}^*$  observables in Table 3; we also show the synthetic line profiles and light curves in Figure 5 and the relative abundance of  $\text{He}^*$  as a function of radius in Figure 6.

The  $\text{He}^*$  line profiles are controlled mainly by the FUV (adverse effect) and the EUV bands (positive effect); the LW and X-ray bands only play minor roles under the “typical” host star conditions. More specifically, the relative abundance of  $\text{He}^*$  is suppressed by soft FUV because it photoionizes the  $\text{He}^*$  states, thus significantly reducing its population and the  $\text{He}^*$  absorption depth. In model 69-1 ( $\times 10$  soft FUV flux), the overall mass-loss rate is enhanced by a few percent thanks to extra energy deposited into the atmosphere. However, the stronger soft FUV flux significantly lowered the number density of  $\text{He}^*$  at a larger radial extent ( $r \gtrsim 20 R_\oplus$ ). The  $\text{He}^*$  line profile depth and the light-curve depth are both reduced by about a factor of two (3.16 to 1.75  $\text{\AA}$ ). The line width also decreased (FWHM from 17.3 down to 14.0  $\text{\AA}$ ) because the high-altitude region with a higher velocity dispersion contributes less to the  $\text{He}^*$  extinction.

In model 69-2 ( $\times 10$  LW flux) the  $\text{He}^*$  observables are mostly unaltered from the fiducial model. This is because the LW band is intrinsically narrow and thus only amounts to a very small fraction of the overall high-energy radiation flux. Moreover, most molecular  $\text{H}_2$  is already dissociated at  $\sim 10^4$  K in our simulations.

At higher EUV fluxes (models 69-3 and 69-4), the much faster outflows not only bring more  $\text{He}^*$  into the exosphere but

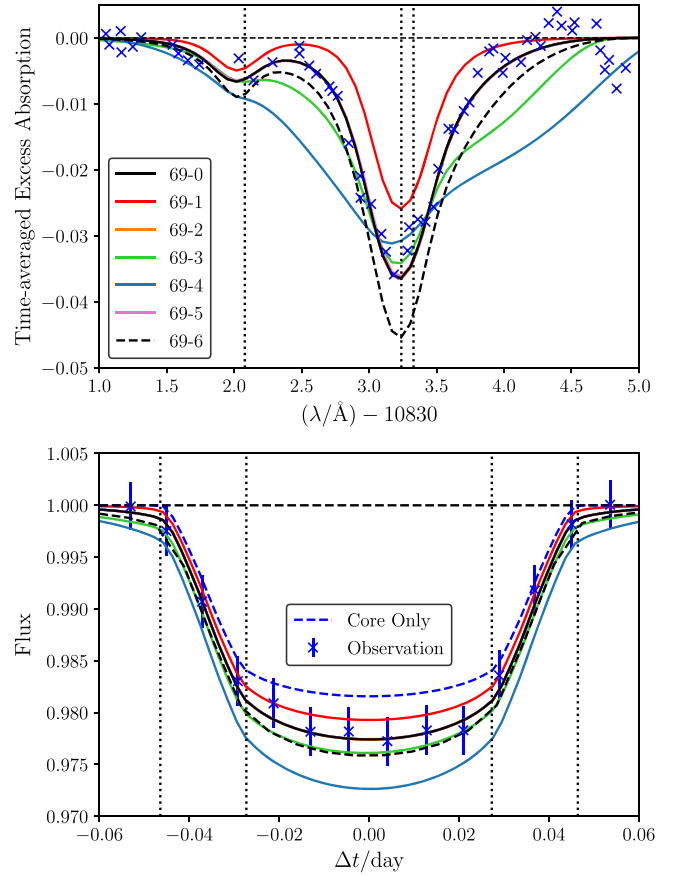


**Figure 5.** Similar to Figure 3, but for models 69-0 through 69-6 in Table 3. The fiducial model 69-0 is also included for reference. Note that models 69-2 and 69-5 are almost fully overlapped with model 69-0.

also spread them out in velocity space, effectively broadening the line profiles. This confirms our earlier picture that EUV flux is most effective in driving photoevaporative outflows (WD18).

Finally, X-ray seems to play a secondary role in photoevaporation and  $\text{He}^*$  observables. Model 69-5 ( $\times 10$  X-ray flux) has very similar observables to the fiducial model. Although X-ray photons are very energetic, they also have much smaller

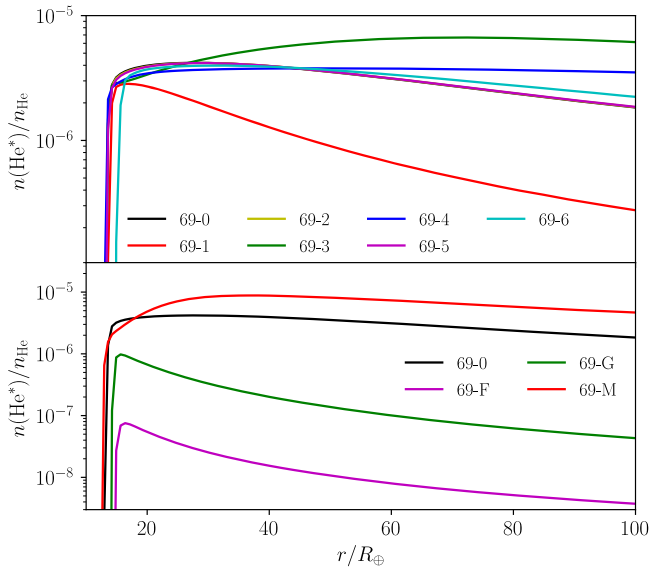


**Figure 6.** Relative abundance profiles of  $\text{He}^*$  (relative to the total helium nucleus density  $n_{\text{He}}$ ), measured along the radial line with  $\theta = \pi/4$ ,  $\phi = 0$  in each simulation domain, for models described in Table 3. The top panel shows models 69-0 and 69-1 through 69-6, while the bottom panel specifically compares the results of different types of host stars (model 69-0 for the K star WASP-69, and models 69-F, 69-G, and 69-M for F, G, and M stars, respectively).

cross sections than EUV photons. As a result, X-rays penetrate deeper into the atmosphere, where collisional processes and dust particles quickly convert the X-ray energies to infrared radiation that escapes easily. This limits the heating potential of X-ray. We reached a similar conclusion in WD18.

### 4.3. Host Spectral Type

Among the handful of reported  $\text{He}^*$  detections, four out of six are planets around K-type hosts (Spake et al. 2018; Venzmer & Bothmer 2018; Allart et al. 2018; Salz et al. 2018; Ninan et al. 2020; Alonso-Floriano et al. 2019). Oklopčić (2019) confirmed that K stars, at least in 1D isothermal models, may be at the sweet spot of FUV/EUV flux balance that best promotes the  $\text{He}^*$  population and thus observability. This section reevaluates such a claim with our 3D hydrodynamic simulation coupled with self-consistent thermodynamics and radiative transfer.

We set up three additional models 69-F, 69-G, and 69-M, whose luminosities in different high-energy bins emulate typical F-type, G-type, and M-type main-sequence stars based on the compilation of Oklopčić (2019); see also Figure 7. We remind the reader that the fiducial model 69-0 has a K-star SED. The flux in each high-energy bin is summarized in Table 2). Broadly speaking, F-type and G-type stars output similar levels of soft and hard EUV fluxes to K-type stars; however, their FUV luminosities are significantly higher by a factor of  $\sim 3000$  and  $\sim 130$ , respectively. For a typical M star, fluxes in all high-energy bands are lower by about one order of magnitude.

$\text{He}^*$  observables of these models are summarized in Table 3 for their mass-loss rates and a few key diagnostics, etc. We show the line profiles and light curves in Figure 8 and the radial distribution of  $\text{He}^*$  in Figure 6. With a soft FUV flux  $\sim 3000$  times higher than our fiducial model, F-type stars significantly suppress the population and observability of  $\text{He}^*$  with an EW

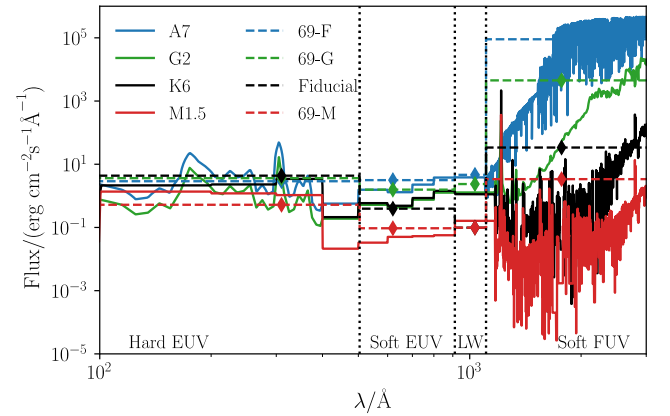


**Figure 7.** SEDs of the incident high-energy photon fluxes, for the models with type F, G, K, and M host stars (models 69-F, 69-G, fiducial model 69-0, and 69-M), presented with dashed lines. Diamonds overplotted on the dashed lines mark the exact energy of incident photons in the simulations (as representatives of the corresponding energy bands; see Section 2.3). For reference, the model spectra of stellar spectral types A7, G2, K6, and M1.5 (based on the compilation in Oklopčić, 2019) are shown with solid curves. Vertical dotted lines mark the boundary between different energy bands: “Hard EUV” for  $h\nu > 24.6$  eV photons that can ionize helium; “Soft EUV” for  $13.6 < (h\nu/\text{eV}) < 24.6$  photons that can ionize hydrogen; “LW” (short for Lyman–Werner) for  $11.2 < (h\nu/\text{eV}) < 13.6$  photons that can photodissociate  $\text{H}_2$ ; “Soft FUV” for  $h\nu < 11.2$  eV photons.

**Table 2**

Radiation Fluxes for Different Model Host Stars Based on the Fiducial Model of WASP-69b

Star Type	$F_{20}$ (2 eV)	$F_{15}$ (7 eV)	$F_{13}$ (12 eV)	$F_{13}$ (20 eV)	$F_{13}$ (40 eV)
F	2.8	$1.6 \times 10^4$	4.7	4.0	2.0
G	1.4	$8 \times 10^2$	2.4	2.0	2.5
M	0.11	0.6	0.1	0.12	0.36

**Note.** For simplicity,  $F_N(h\nu) \equiv F(h\nu)/(10^N \text{cm}^{-2} \text{s}^{-1})$ , calibrated for the value at the planet orbit without any extinction.

reduced by almost two orders of magnitude ( $3.16\text{--}0.04 \text{ \AA}$ ). However, the mass-loss rate of the photoevaporative outflow is similar to that of the fiducial model. Again, photoevaporation is driven mostly by EUV, which has similar flux levels between F and K stars. On the other hand, for a typical M-star host, whose higher-energy flux levels are weaker in all bands, the mass-loss rate is reduced by one order of magnitude. Nonetheless, the EW of  $\text{He}^*$  in the transmission spectrum only declines by a factor of 2 ( $3.16\text{--}1.4 \text{ \AA}$ ). Again, this is because its much weaker soft FUV flux allows proportionally more  $\text{He}^*$  to exist in the outflow (Figure 6). A G star represents some middle ground; its  $\sim 130$  times higher soft FUV flux suppresses the EW  $\text{He}^*$  by a factor of 6.

In summary, our findings suggest that K-star planet hosts are indeed favorable targets for  $\text{He}^*$  observations, consistent with the suggestion of Oklopčić (2019). The high-energy SED, nonetheless, is expected to change significantly as a function of host star age and activity level. The suppression factors of  $\text{He}^*$  around G- and M-type stars are often only a factor of a few. We encourage observers to keep them in their target list, particularly the young and active ones. We also predict that there will be more reports of  $\text{He}^*$  detection around G- and M-type hosts soon. Another important point we would like to

**Table 3**  
Results of Various Models, Based on the Fiducial Model for WASP-69b

Model	Description	$\dot{M}$ ( $10^{-9} M_{\oplus} \text{ yr}^{-1}$ )	$\langle W_{\lambda} \rangle$ ( $10^{-2} \text{ \AA}$ )	$\Delta v_{\text{peak}}^a$ ( $\text{km s}^{-1}$ )	FWHM <sup>b</sup> ( $\text{km s}^{-1}$ )
69-0	3D fiducial	0.55	3.16	-2.1	17.3
69-0-2D	2D test (fiducial parameters)	0.56	3.10	-2.0	16.6
69-0-1D	1D test (fiducial parameters)	0.69	3.14	0.07	16.2
69-1	10×Flux for soft FUV ( $h\nu = 7 \text{ eV}$ )	0.61	1.75	-1.7	14.0
69-2	10×Flux for LW ( $h\nu = 12 \text{ eV}$ )	0.56	3.18	-2.1	17.4
69-3	10×Flux for soft EUV ( $h\nu = 20 \text{ eV}$ )	0.66	4.13	-2.4	24.2
69-4	10×Flux for hard EUV ( $h\nu = 40 \text{ eV}$ )	2.50	5.62	-3.8	48.1
69-5	10×Flux for X-ray ( $h\nu = 3 \text{ keV}$ )	0.55	3.12	-2.0	17.6
69-6	1/2 planet mass ( $M_p = 41.3 M_{\oplus}$ )	0.93	4.25	-2.1	17.2
69-F	Fiducial model with F-type host	0.70	0.04	-0.8	9.0
69-G	Fiducial model with G-type host	0.64	0.51	-1.5	10.3
69-M	Fiducial model with M-type host	0.05	1.40	-0.6	12.9

**Notes.** The values are time averages taken over the last  $15 \tau_{\text{dyn}}$  of the simulations. Fluctuations are negligible for all models in the table.

<sup>a</sup> Shifts (positive values for redshifts and vice versa) of the right-hand-side peaks in the velocity space, compared to the line-ratio-averaged line center of  $\lambda = 10833.29 \text{ \AA}$ .

<sup>b</sup> FWHM of the longer-wavelength peak in the velocity space.

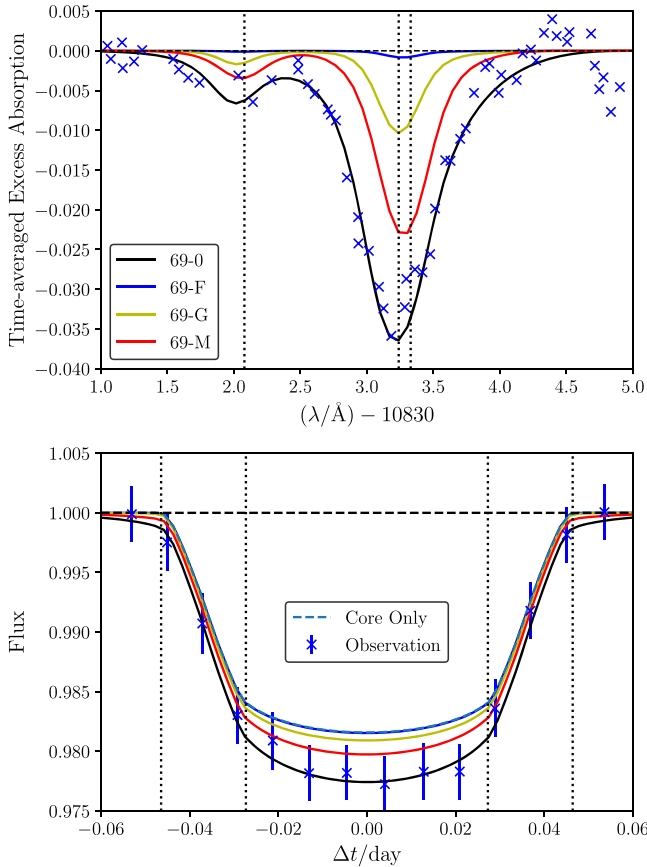


**Figure 8.** Similar to Figures 3 and 5, but presenting models 69-F, 69-G, and 69-M for different host star spectral types in Table 3. Note that the fiducial model 69-0 has a K star.

stress is that the depth of the  $\text{He}^*$  line profile cannot be translated to the underlying mass-loss rate without knowing the high-energy SED of the host star. In other words, measuring

the XUV SED of the host star directly is crucial for correctly interpreting the  $\text{He}^*$  observations.

#### 4.4. Surface Gravity

The mass-loss rate of photoevaporation depends quite strongly on the depth of the gravitational potential well of the planet. A shallower potential allows faster outflow with the same high-energy irradiation. In model 69-6 we adjusted the planet interior such that the planet mass is reduced by half while keeping the transit radius the same. This effectively lowers the surface gravity of the planet by a factor of two. The mass-loss rate in model 69-6 increases to  $\dot{M} \simeq 9.3 \times 10^{-10} M_{\oplus} \text{ yr}^{-1}$ , which is  $\sim 70\%$  larger than the fiducial model. This larger mass-loss rate can be decomposed into an increase in the terminal outflow velocity by  $\sim 10\%$  and an increase of the outflow density by  $\sim 60\%$ .

The  $\text{He}^*$  line profile depth responds to this increase of mass-loss rate sublinearly. In Figure 5, the line profile has  $\sim 40\%$  larger depth than that in the fiducial model, while the EW increases by about  $\sim 30\%$ . However, the  $\text{He}^*$  line profile maintains a similar morphology with the peak velocity shift and the FWHM unchanged from the fiducial model (Table 3). In short, puffier, low surface gravity planets are more likely to undergo strong photoevaporative mass loss and should prove great targets for  $\text{He}^*$  observations.

## 5. Discussions

### 5.1. Equivalent Widths

Photometric measurement of transits, compared to transmission spectra, features much lower costs of exposures and higher viability if one wants to study atmospheric dispersal processes over an ensemble of planets statistically. Our numerical experiments within and beyond this paper have indicated that the excess absorption by metastable helium atoms in the  $\tau \lesssim 1$  outskirts plays an important role in casting the transmission features (e.g., Figure 4). The EW at a given orbital phase angle

$\Phi$  can be reasonably approximated by (using Equations (2) and (3))

$$\begin{aligned} W_\lambda &= \int d\lambda \left[ 1 - \int d\Sigma S e^{-\tau(\lambda; \Phi)} \right] \\ &\simeq \int S d\Sigma \int d\lambda \tau(\lambda) \\ &\propto \int d\Sigma \int_{\text{LoS}} |dx| n(\text{He}^*) \int d\lambda \sum_i \sigma_i(\lambda) \\ &\propto \int dV n(\text{He}^*). \end{aligned} \quad (6)$$

Here we ignored limb darkening and stellar rotation, and the last integration measure  $dV$  runs through the volume spanned by all LOSs over the projected stellar surface. Note that the integration  $\int d\lambda \sigma(\lambda)$  is a constant regardless of thermal broadening or bulk velocity shifts. This expression is still valid under time averaging.

EWs of transmission spectra, which are equivalent to transit depths up to a conversion relation, are most relevant to stellar irradiation. Unless the FUV flux is too intense, it is a reasonable approximation for order-of-magnitude estimations about the total  $\text{He}^*$ , in which the  $n(\text{He}^*)/n_{\text{H}}$  ratio is mostly invariant throughout a relatively large range of radii (see Sections 4.2 and 4.3 and, e.g., Oklopčić 2019). If valid, these approximated expressions enable the EW as a good indicator of the materials that stay in front of the host star and a reasonable representative of the outflow as a whole. In addition, unless significant impact is coming from the host star, dimensionality effects mostly change the distribution of absorbers in the configuration and velocity space but are less relevant to the EW (e.g., Table 1). In these cases, the integrated EW can be consistently predicted by reasonable 2D or even 1D calculations and hence reduce the costs of numerical calculations once data-driven modeling is desired.

Admittedly, EW observation would still suffer from the losses in accuracy to constrain the physics of host stars. The first issue is the degeneracy of parameters. Roughly speaking, soft FUV photons ( $h\nu > 4.8$  eV) destruct metastable helium and lower the  $n(\text{He}^*)/n_{\text{H}}$  ratio, while EUV photons enhance the EW mainly by launching stronger photoevaporative outflows. Stellar winds that are sufficiently strong can also concentrate materials (including  $\text{He}^*$ ) inside the cylinder above the projected stellar surface and thus raise the EW (we refer the reader to Wang & Dai 2021, hereafter Paper II, for more thorough discussions). The second issue is that the sublinear dependence of EW on stellar irradiation, mainly due to the interconnectivity of thermochemical networks, makes EW alone a less sensitive parameter. These issues can be partially solved by introducing other measurements (such as HST STIS for FUV in Loyd et al. 2016), to eliminate the degeneracy.

### 5.2. Interpreting Transmission Spectra and Light Curves

Spectral line shapes can be good representatives of photoevaporation structures. It should be noticed that, even though hard EUV photons ( $h\nu > 24.6$  eV) produce  $\text{He}^+$  as the most important progenitor to populate the  $2^3S$  state, this effect is likely to saturate before the hard EUV flux becomes intermediately intense (e.g., Section 4.2) and thus does *not* affect the ratio  $n(\text{He}^*)/n_{\text{He}}$  directly. EUV radiation affects the appearance of planetary outflows more by controlling the kinematics and shaping the spectral line. As the key component of launching photoevaporation, stronger EUV flux typically drives faster winds, spreading  $\text{He}^*$  atoms wider in the

velocity space and broadening the spectral lines. Combining this extra dimension of velocity information with the transit depths or EWs (Section 5.1; Equation (6)), reasonable estimations of atmospheric mass-loss rates can be established. Such estimations should be most robust for planets with FUV-weak K-type and M-type main-sequence stars. For host stars with excessive FUV irradiation, accounting for the FUV-dominated  $\text{He}^*$  destruction by other observation measures is demanded (similar to Section 5.1).

We emphasize that full 3D hydrodynamic-thermochemical simulations are demanded to interpret the characteristics in spectra and light curves accurately. First, as was elaborated in WD18, the consistency of modeling photoevaporation requires multidimensional nonequilibrium thermochemical calculations, which are inevitable to account for an intertwined system of physical processes, including heating, cooling, chemical reactions, and even ray-tracing. Second, understanding temporal and spectral observations requires knowledge about the distribution of the concerned tracer ( $\text{He}^*$ ) in both configuration and momentum spaces. Simplified steady-state 1D spherical symmetric calculations have to assume isotropic geometry, but actual streamlines and stellar photons never move radially. The difference in hydrodynamic conditions (esp. gas temperature) between the day and night hemispheres causes latitudinal advection beyond 1D models. What is more, the outflows of close-in planets can be considerably modulated by stellar gravity and orbital motion, which cannot be appropriately handled even with 2.5D axisymmetric simulations. Moreover, there are various systems showing prominent gaseous tails in light curves, which denies the possibility of improper calculations that are simpler than 3D. We postpone the discussions about these complicated interactions to Paper II. Nevertheless, we still emphasize that 3D simulations should eventually reward us with consistent and thorough understandings of the physics that transmission spectrum observations should be able to bring about.

### 5.3. Variability and Stellar Flares

During one of the transits of WASP-69b in Nortmann et al. (2018), the  $\text{He}^*$  line profile experienced a  $\sim 30\%$  drop in magnitude that lasted for about 20 minutes. This variability could well be instrumental in origin, but here we explore an alternative explanation that it is generated by a stellar flare on the host star.

Solar/stellar flares are associated with the surface magnetic activity of the host star. Their amplitudes can range below a percent to even orders of magnitude in extreme cases (“superflares”; see Günther et al. 2020, and references therein). The sudden rise of luminosity is often followed by exponential decays to nominal flux level on timescales of minutes or hours. To investigate the consequences of flaring events on  $\text{He}^*$  observables, we first inject a simple flare model in which fluxes across *all* energy bands increase by a factor of 10 and 100, which then quickly decay to the quiescent state exponentially with a timescale of 500 s.

The temporal response of our fiducial model to these flares is shown in Figure 9. Independent of the energy injected, the common mode of response is as follows. Before the dynamics of the outflowing atmosphere can fully respond to the flares, the photoionization of  $\text{He}^*$  by soft FUV photons reduces the number density of  $\text{He}^*$  and causes a significant decrease in the EW. It is only after the dynamical timescale  $t - t_{\text{flare}} \sim \tau_{\text{dyn}} \sim$  hours that the flare-generated surge of photoevaporative mass loss reaches the higher altitudes where most of  $\text{He}^*$  absorption

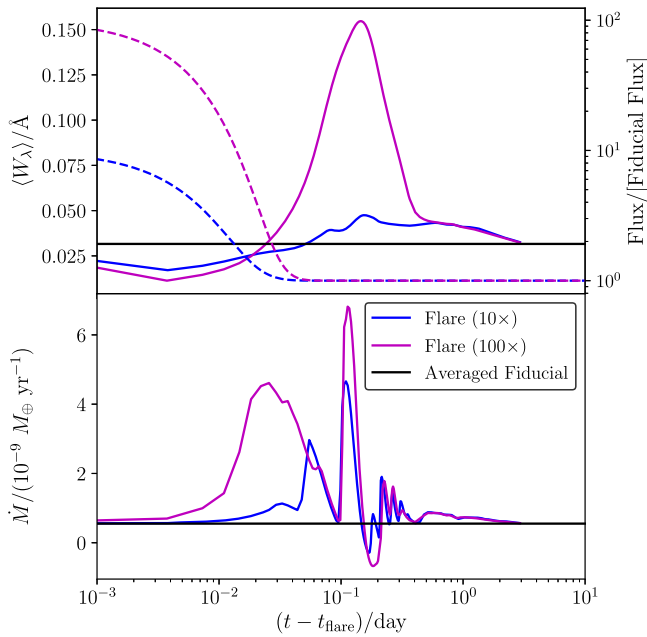


**Figure 9.** Temporal variations of the two models (based on model 69-0) with flares that increase all high-energy radiation by 10 and 100 times uniformly (Section 5.3). The top panel shows the EWs of the metastable helium absorption by solid curves. The two dashed lines, which should read the right ordinate, indicate the evolution of radiation fluxes in all energy bands. The mass-loss rates are shown in the bottom panel. Time-averaged values for the fiducial model are also plotted for reference.

occurs. As a result, the EW of  $\text{He}^*$  increases after the first hour or so and remains high for several hours. Looking at the mass-loss rate across the outer boundary of the simulation (bottom panel of Figure 9), it experiences several oscillations on dynamical timescales as the systems respond to the increased flux from the flare. The EW and other observables, however, are the spatially integrated quantities; thus, EW effectively smears out most of these oscillations and has a much smoother variation (top panel of Figure 9). Comparing with variability seen in WASP-69b (Nortmann et al. 2018), a flare that simultaneously raises all high-energy radiation does not appear to be a good explanation. This is because it should be observed as a decrease followed by an increase of  $\text{He}^*$  absorption rather than the decrease only in the observations (Nortmann et al. 2018).

We therefore explore a different flare model in which *only* the soft FUV band surges. We do not have observational support that flares of this kind exist. We explore this rather contrived scenario just out of curiosity. Remember from Section 4.2 that the soft FUV primarily suppresses the  $\text{He}^*$  abundance by photoionization without significantly changing the overall kinematics. A soft-FUV-only flare may produce the observed decrease of  $\text{He}^*$  line depths. We set up three extra simulation runs, again based on the fiducial model of WASP-69b. We put in soft FUV flares (10, 100 and 1000 times the nominal value) that start at the middle of the transits and last for 30 minutes. In Figure 10, we can see that the light curves respond to these soft-FUV-only flares quickly. In order to reproduce the  $\sim 30\%$  variation, a soft FUV flare between 10 and 100 $\times$  the nominal level is required. This should be readily observable in the Ca II H and K lines of the CARMENES spectra in Nortmann et al. (2018). Nevertheless, enhanced activity was not observed in the spectra during or preceding the observed light-curve variation (private communications,

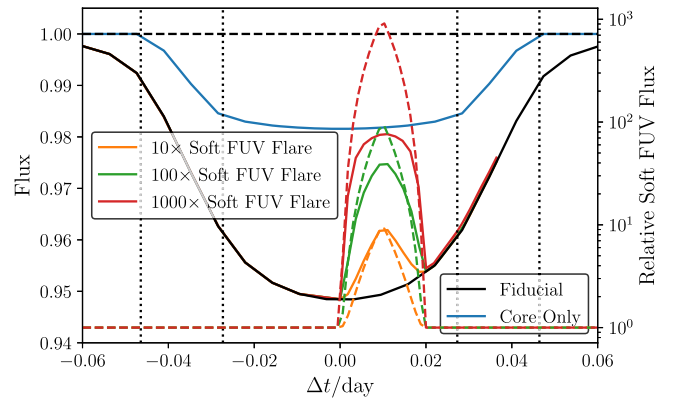


**Figure 10.** Similar to the bottom panel of Figure 3, showing the light curves following soft-FUV-only flares that start at midtransit ( $\Delta t = 0$ ) and terminate after 0.5 hr. Different flare intensities are indicated by colors. The light curves in solid lines should read the left ordinate, while the dashed lines are the flare shapes and should be read with the right ordinate. Soft FUV only destroys  $\text{He}^*$ , while it does not significantly perturb the photoevaporative outflow; thus, it only produces a decrease in  $\text{He}^*$  line depth that is seen in WASP-69b. Nonetheless, we do not believe that this is the explanation for the observed variability (see Section 5.3 for details).

Nortmann). After all, stellar flares do not seem to be a viable explanation of the temporal variability seen in the  $\text{He}^*$  line profiles of Nortmann et al. (2018); an instrumental effect is perhaps a better solution.

## 6. Summary

In this work, we simulate the ionized mass loss of close-in exoplanets and the metastable helium ( $\text{He}^*$ ) absorption during the planetary transit. We synthesize spectrally resolved line profiles and the light curves in a narrow filter band around the  $\text{He}^*$  transitions. Dynamics of such synthesis requires 3D hydrodynamic simulations of photoevaporating planetary atmospheres, in which nonequilibrium thermochemistry and ray-tracing radiative transfer are coevolved with the hydrodynamics. The processes that populate and depopulate the metastable state of neutral helium are included in a thermochemical network and solved efficiently on GPUs.

With reasonable assumptions about the system parameters and high-energy SED of WASP-69, we find a plausible model that launches a photoevaporative outflow with a mass-loss rate of  $\dot{M} \simeq 5.5 \times 10^{-10} M_{\oplus} \text{ yr}^{-1} \simeq 1.0 \times 10^{11} \text{ g s}^{-1}$ . The model yields a spectrum and a light curve that are in remarkable agreement with the observations in terms of the EW, line ratios, blueshift, and line broadening (Nortmann et al. 2018; Vissapragada et al. 2020). Inside this outflow, metastable helium is formed almost solely by recombination. Its destruction is mainly due to collisional de-excitation at small radii where the density is high, and photoionization by FUV photons at the outer lower-density regions.

With this fiducial model of WASP-69b, we investigated how the photoevaporative outflow and  $\text{He}^*$  observables depend on various input parameters. Simulations in 3D are crucial for capturing the full hydrodynamics including Coriolis force and advection. These effects are needed for producing the correct line profile, including the line ratios, kinematic broadening, and the overall blueshift. We found that EUV photons are most efficient in driving the photoevaporation dynamics and in producing  $\text{He}^+$  as the progenitors of recombination excitation of  $\text{He}^*$ . The soft FUV photons that can ionize  $\text{He}^*$  often play an

adverse effect on the He\* observability. X-ray photons, having much lower interaction cross section, are of secondary importance. Surface gravity also determines the effectiveness of photoevaporative outflows with puffer planets experiencing significantly stronger outflows, but the response of He\* EW is sublinear.

K stars hit the sweet spot of FUV/EUV balance that maximizes the detectability of He\* lines. F or earlier-type stars have excessive FUV fluxes that suppress the He\* lines by orders of magnitude. G and M dwarfs represent a middle ground: He\* lines should still be observable particularly for the younger and more active ones. In any case, the depths of He\* line profiles cannot be translated into mass-loss rates without knowing the host star high-energy SED.

We also investigated whether stellar flares could explain some of the temporal variability of WASP-69b (Nortmann et al. 2018). We found that a flare that enhances all high-energy radiations initially suppresses He\* lines (since FUV photons ionize He\*) before the whole system adjusts to a higher mass-loss state after some dynamical timescales (usually a few hours). This characteristic shape is not consistent with the observed temporal variability of WASP-69b, which only shows a decline of He\* line depth before returning to nominal levels. Stellar flares are unlikely to be the explanation for this type of variability.

This work is supported by the Center for Computational Astrophysics of the Flatiron Institute and the Division of Geological and Planetary Sciences of the California Institute of Technology. L.W. acknowledges the computing resources provided by the Simons Foundation and the San Diego Supercomputer Center. We thank our colleagues (in alphabetical order) Philip Armitage, Zhuo Chen, Jeremy Goodman, Xiao Hu, Heather Knutson, Mordecai Mac-Low, Jessica Spake, Kengo Tomida, Songhu Wang, Andrew Youdin, and Michael Zhang, for helpful discussions and comments. We especially thank Shreyas Vissapragada for detailed suggestions and discussions. We particularly thank the anonymous referee for the constructive comments and suggestions.

## Appendix Cores and Internal Atmospheres of Model Planets

Gas giants like WASP-69b may have degenerate hydrogen and helium in their interior. We adopt the EOSs tabulated by Miguel et al. (2016), which describe the behaviors of hydrogen and helium over wide ranges of pressure and temperature, from the degenerate states to ideal gases. Those tabulated EOSs present the density and entropy of hydrogen and helium as functions of temperature and pressure. The combined EOS for a mixture of hydrogen and helium at a fixed atom number fraction  $x_{\text{H}}$  is given by solving the equation for  $x_{p,\text{H}}$  (the partial pressure of hydrogen),

$$\frac{m_{\text{H}}x_{\text{H}}}{m_{\text{He}}(1 - x_{\text{H}})} = \frac{\rho_{\text{H}}(p, x_{p,\text{H}}, T)}{\rho_{\text{He}}[p(1 - x_{p,\text{H}}), T]}, \quad (\text{A1})$$

in which  $p$  is the total pressure,  $T$  is the temperature,  $m_{\text{H}}$  and  $m_{\text{He}}$  are the atomic masses of hydrogen and helium, respectively, and  $\rho_{\text{H}}$  and  $\rho_{\text{He}}$  are interpolated from the EOS tables. The overall density then reads  $\rho = \rho_{\text{H}} + \rho_{\text{He}}$ . The entropy density  $s$  of the materials is also calculated, so that we can obtain the adiabatic

gradient,

$$\nabla_{\text{ad}} \equiv \left( \frac{\partial \ln p}{\partial \ln T} \right)_s = - \frac{(\partial \ln s / \partial \ln p)_T}{(\partial \ln s / \partial \ln T)_p}. \quad (\text{A2})$$

Note that the entropy of mixing does not affect these derivatives.

The spherical symmetric isentropic hydrostatics are calculated by solving a boundary value problem for the set of ODEs:

$$\begin{aligned} \frac{dp}{dr} &= - \frac{GM\rho}{r^2}, & \frac{dM}{dr} &= 4\pi r^2 \rho, \\ \frac{dT}{dr} &= \nabla_{\text{ad}} \left( \frac{T}{p} \right) \left( \frac{dp}{dr} \right), \end{aligned} \quad (\text{A3})$$

where  $M$  denotes the mass enclosed by radius  $r$ . Specifying the boundary conditions  $(p_c, T_c)$  as the “eigenvalues,” we can integrate these ODEs from the boundary of a dense solid core with radius  $r_c$  and given mass  $M_c$  up to the radiative–convective boundary  $r = r_{\text{rcb}}$ . At  $r_{\text{rcb}}$  the temperature approaches the equilibrium temperature of the quasi-isothermal layer  $T = T_{\text{eq}}$ . Thus, the convective inner atmosphere is smoothly connected to a quasi-isothermal outer atmosphere whose density profile obeys ( $\mu$  is the dimensional mean molecular mass)

$$\rho = \rho_{\text{rcb}} \exp \left[ \left( \frac{GM_{\text{rcb}}\mu}{r_{\text{rcb}}k_{\text{B}}T_{\text{eq}}} \right) \left( \frac{r_{\text{rcb}}}{r} - 1 \right) \right]. \quad (\text{A4})$$

The density profile is then used to calculate the effective transiting radius,

$$\langle r_{\text{eff}} \rangle = \left\{ \frac{1}{\pi} \int_0^{r_{\text{cut}}} db \, 2\pi b [1 - e^{-\tau(b)}] \right\}^{1/2}, \quad (\text{A5})$$

where  $r_{\text{cut}}$  is an arbitrary cutoff size (to calculate the effective transiting radius in the broad optical band, we use  $r_{\text{cut}} = 100 R_{\oplus}$ ),  $\tau(b)$  is the optical depth along the LOS at impact parameter  $b$ ,

$$\tau(b) \equiv \int_{-r_{\text{cut}}}^{r_{\text{cut}}} dz \, \sigma n|_{r=\sqrt{b^2+z^2}}, \quad (\text{A6})$$

$n$  is the number density of the extinction particle, and  $\sigma$  is the extinction cross section per particle. The eigenvalues  $(p_c, T_c)$  are searched iteratively until both  $M_{\text{rcb}}$  and  $\langle r_{\text{eff}} \rangle$  match the observed mass  $M_{\text{p}}$  and optical transiting radius  $R_{\text{p}}$  of the planet being simulated. In all models discussed in this paper, for simplicity we assume that there are no rocky cores ( $r_c = 0$ ,  $M_c = 0$ ). This assumption hardly affects the properties of the upper atmosphere. We also use the  $\kappa$  of the Thomson scattering to estimate  $\langle r_{\text{eff}} \rangle$ . We have also tested other plausible values of opacity (e.g., the optical  $\kappa$  for  $r_{\text{dust}} = 5 \text{ \AA}$  very small grains with  $10^{-4}$  dust-to-gas mass ratio) and found that  $\langle r_{\text{eff}} \rangle$  varies by only  $\sim 2\%$  under the same boundary conditions. Again, the specific choice of opacity hardly affects the upper atmosphere.

## ORCID iDs

Lile Wang  <https://orcid.org/0000-0002-6540-7042>

Fei Dai  <https://orcid.org/0000-0002-8958-0683>

## References

- Allart, R., Bourrier, V., Lovis, C., et al. 2018, *Sci*, 362, 1384  
Alonso-Floriano, F. J., Snellen, I. A. G., Czesla, S., et al. 2019, *A&A*, 629, A110

- Anderson, D. R., Collier Cameron, A., Delrez, L., et al. 2014, *MNRAS*, **445**, 1114
- Bourrier, V., Ehrenreich, D., & Lecavelier des Etangs, A. 2015, *A&A*, **582**, A65
- Drake, G. 2006, High Precision Calculations for Helium (New York: Springer Science+Business Media Inc.), 199
- Drake, G. W. 1971, *PhRvA*, **3**, 908
- Edwards, S., Fischer, W., Kwan, J., Hillenbrand, L., & Dupree, A. K. 2003, *ApJL*, **599**, L41
- Ehrenreich, D., Bourrier, V., Wheatley, P. J., et al. 2015, *Natur*, **522**, 459
- France, K., Loyd, R. O. P., Youngblood, A., et al. 2016, *ApJ*, **820**, 89
- Fulton, B. J., Petigura, E. A., Howard, A. W., et al. 2017, *AJ*, **154**, 109
- Ginzburg, S., Schlichting, H. E., & Sari, R. 2016, *ApJ*, **825**, 29
- Ginzburg, S., Schlichting, H. E., & Sari, R. 2018, *MNRAS*, **476**, 759
- Gong, M., Ostriker, E. C., & Wolfire, M. G. 2017, *ApJ*, **843**, 38
- Gorti, U., & Hollenbach, D. 2008, *ApJ*, **683**, 287
- Gudel, M. 1992, *A&A*, **264**, L31
- Günther, M. N., Zhan, Z., Seager, S., et al. 2020, *AJ*, **159**, 60
- Gupta, A., & Schlichting, H. E. 2019, *MNRAS*, **487**, 24
- Gupta, A., & Schlichting, H. E. 2020, *MNRAS*, **493**, 792
- Kirk, J., Alam, M. K., López-Morales, M., & Zeng, L. 2020, *AJ*, **159**, 115
- Kulow, J. R., France, K., Linsky, J., & Loyd, R. O. P. 2014, *ApJ*, **786**, 132
- Kwan, J., Edwards, S., & Fischer, W. 2007, *ApJ*, **657**, 897
- Lampón, M., López-Puertas, M., Lara, L. M., et al. 2020, *A&A*, **636**, A13
- Lecavelier Des Etangs, A., Ehrenreich, D., Vidal-Madjar, A., et al. 2010, *A&A*, **514**, A72
- Leighly, K. M., Dietrich, M., & Barber, S. 2011, *ApJ*, **728**, 94
- Loyd, R. O. P., France, K., Youngblood, A., et al. 2016, *ApJ*, **824**, 102
- Miguel, Y., Guillot, T., & Fayon, L. 2016, *A&A*, **596**, A114
- Müller, B., Tauris, T. M., Heger, A., et al. 2019, *MNRAS*, **484**, 3307
- Nakamura, K., Takiwaki, T., & Kotake, K. 2019, *PASJ*, **71**, 98
- Ninan, J. P., Stefansson, G., Mahadevan, S., et al. 2020, *ApJ*, **894**, 97
- Nortmann, L., Pallé, E., Salz, M., et al. 2018, *Sci*, **362**, 1388
- Oklopčić, A. 2019, *ApJ*, **881**, 133
- Oklopčić, A., & Hirata, C. M. 2018, *ApJL*, **855**, L11
- Owen, J. E., & Wu, Y. 2016, *ApJ*, **817**, 107
- Owen, J. E., & Wu, Y. 2017, *ApJ*, **847**, 29
- Palle, E., Nortmann, L., Casasayas-Barris, N., et al. 2020, *A&A*, **638**, A61
- Rafikov, R. R. 2006, *ApJ*, **648**, 666
- Salz, M., Czesla, S., Schneider, P. C., et al. 2018, *A&A*, **620**, A97
- Seager, S., & Sasselov, D. D. 2000, *ApJ*, **537**, 916
- Spake, J. J., Sing, D. K., Evans, T. M., et al. 2018, *Natur*, **557**, 68
- Stone, J. M., Tomida, K., White, C. J., & Felker, K. G. 2020, *ApJS*, **249**, 4
- Tielens, A. G. G. M., & Hollenbach, D. 1985, *ApJ*, **291**, 722
- Tsiaras, A., Waldmann, I. P., Zingales, T., et al. 2018, *AJ*, **155**, 156
- Turner, J. D., Christie, D., Arras, P., Johnson, R. E., & Schmidt, C. 2016, *MNRAS*, **458**, 3880
- Venzmer, M. S., & Bothmer, V. 2018, *A&A*, **611**, A36
- Vidal-Madjar, A., Lecavelier des Etangs, A., & Désert, J. M. 2003, *Natur*, **422**, 143
- Vissapragada, S., Knutson, H. A., Jovanovic, N., et al. 2020, *AJ*, **159**, 278
- Wahl, S. M., Hubbard, W. B., Militzer, B., et al. 2017, *GeoRL*, **44**, 4649
- Wang, L., & Dai, F. 2018, *ApJ*, **860**, 175
- Wang, L., & Dai, F. 2021, *ApJ*, **914**, 99
- Wang, L., & Goodman, J. 2017, *ApJ*, **847**, 11
- Youngblood, A., France, K., Loyd, R. O. P., et al. 2016, *ApJ*, **824**, 101
- Youngblood, A., France, K., Loyd, R. O. P., et al. 2017, *ApJ*, **843**, 31